

generation battery with high theoretical energy densities (ex: Li-S, 2567 W h kg⁻¹).² Lithium (Li) metal also offers high gravimetric capacities (3860 mA h g⁻¹) and low reduction potentials (-3.04 V vs. S.H.E.).² Yet, developments in LMBs have been limited by various issues, including the corrosion of the highly reactive Li metal and the formation of high surface area, inhomogeneous Li deposits, known as dendrites, at the anode.^{2,3}

Two properties that significantly affect the performance of the LMBs are the composition of the solid electrolyte interphase (SEI) and the morphology of the Li deposited at the anode.⁴ The SEI is formed from decomposed electrolyte and Li and is a Li-ion conducting, chemically passivating layer at the anode-electrolyte interface. While passivation provided by the SEI can improve cycle life, the SEI can be fractured by deposited Li, leading to hot spots for Li metal dendrite growth and the associated electrolyte consumption to form new SEI. Thus, SEIs that are mechanically robust, electrochemically stable, and homogeneous are favored. Studies have shown that such SEIs are attained *via* the incorporation of inorganic species primarily derived from the anion of the salt in the electrolyte.⁵⁻¹⁰

With each cycle, Li electrodeposits on the anode current collector and its morphology evolves. Low surface area Li deposits are beneficial because they limit the interaction between the Li metal and the electrolyte, preventing adverse reactions between Li and electrolyte.¹¹ Additionally, dense and homogenous Li deposits are preferred because they prevent localized ion fluxes that can perpetuate SEI fracturing, generate dendrite growth, and produce electronically isolated Li/dead Li.¹² Thus, various methods have been employed to control the morphology of the Li deposition including electrolyte engineering,^{9,13,14} stable host design,¹⁵⁻¹⁸ and surface engineering. Furthermore, surface engineering has been leveraged to improve Li deposition *via* the use of lithiophilic and reactive surfaces amongst other routes.¹⁹⁻²² Particularly, the application of atomic layer deposition (ALD) and molecular layer deposition (MLD), two techniques that use sequential and self-limiting gas-surface reactions to form conformal and uniform thin films, have been applied to change the interfacial properties of batteries and create surfaces conducive to the formation of dense and compact Li deposits.²³⁻²⁵ Interfacial coatings deposited using ALD have also been utilized to modulate SEI decomposition reactions.²⁶⁻²⁸ ALD deposited interfacial films thus present a unique opportunity to regulate reactions at key interfaces that influence SEI composition, Li deposition, and electron transfer to provide a deeper understanding of fundamental battery operation, as well as suggest new avenues for improving performance.

Counterintuitive to the general concept of nucleation, our group has shown that ALD-grown, electrically resistive thin films support the growth of dense low surface area Li deposits on the Cu current collector resulting in major performance benefits in LMB systems.^{4,29} Although the resistive films impede electron transfer, defects in the film create areas of low resistance. It has been hypothesized that these low resis-

tance defects behave like ultramicroelectrodes and encourage radial diffusion of Li ions to the nuclei, promoting lateral growth and producing low surface area, dense, and planar Li deposits.³⁰ The resistive thin film coatings increase the first-cycle Li nucleation overpotential, making the electrical resistance of the current collector a critical Li morphology modulator, and allowing first-cycle Li nucleation overpotential to serve as a proxy of the resistance measurement. Regarding the practical applicability of resistive thin film coatings, previous research from our group on singular resistive films, including Al₂O₃ and HfO₂, also confirms improved cycling performance in practical anode-free pouch cells.^{4,29}

In the present work, we take advantage of the morphological control that electrical resistance provides to explore the impact of interfacial properties on the SEI composition and the performance of the LMB. This uniquely allows us to understand the impact of SEI composition during kinetic regimes that are typically convoluted by both Li nucleation and SEI growth. Previous studies have focused on extreme cases of morphological control, including ultrafast deposition when electrodeposition is favored over SEI growth,^{31,32} or by contrasting interfaces with drastically different morphologies.³³ We instead explore the convoluted regime present at moderate current densities by creating resistive films of equal resistance, but of different thicknesses and different metal oxides, to maintain a constant 1st cycle Li nucleation overpotential and hence fix the Li nucleation morphology. Holding constant the Li nucleation morphology allows us to explore the impact of thin film chemistry on the SEI. We use ALD to modify the Cu current collector with sub-20 nm resistive thin films, including materials that have been previously applied to interfacial anode modification, such as Al₂O₃ and HfO₂, as well as introducing the use of ZrO₂ and AlHf_xO_y. Aside from creating conformal and uniform thin films, ALD allows us to have effective control over the thin film thickness to ensure fixed resistance. We show through scanning electron microscopy (SEM) results that all cells modified with resistive metal oxide films exhibit resistance-fixed Li nucleation morphology. However, long-term cycling tests reveal differences in cell performance and life cycle.

Through the use of X-ray photoelectron spectroscopy (XPS), we investigate the relative abundance of inorganic species in the SEI, as well as the anion-derived nature of the SEI. We show through a compilation of XPS data that the composition of the SEI is tuned by the surface chemical properties of the thin film. Specifically, each metal oxide has a unique affinity to electrolyte species, which consequently alters electrolyte decomposition and incorporation into the SEI. Additionally, we conduct separate XPS analyses on three types of samples to investigate the SEI composition: 1. on thin film-modified Cu before Li deposition, 2. atop the thin film and Li deposits after the initial Li deposition cycle, and 3. only above the deposited Li by ensuring a high deposition capacity. This analysis confirms that the metal oxide thin film tunes the SEI composition. Furthermore, we create a set of binary stacked metal oxide thin films that maintain the fixed resistance while flipping the



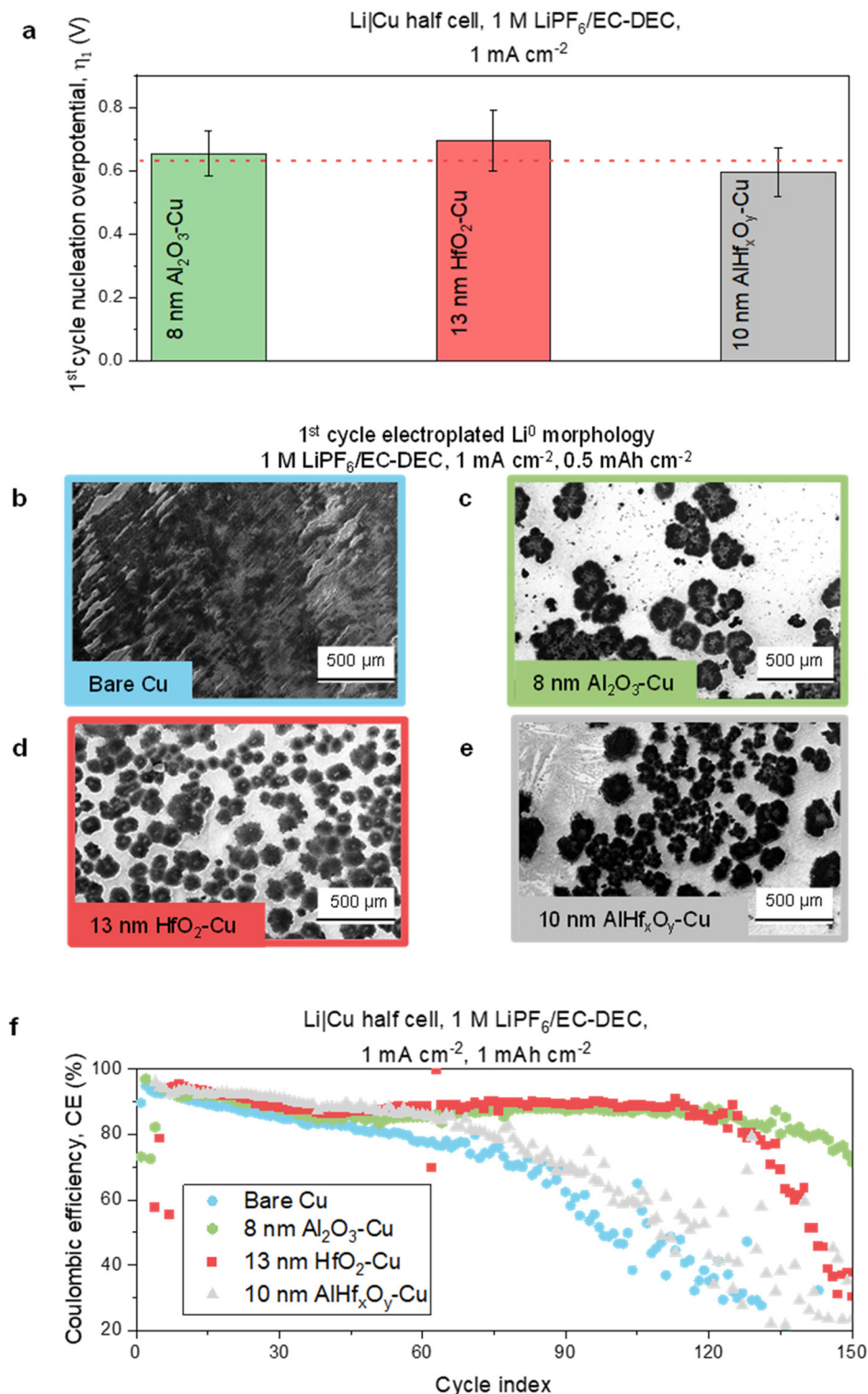


Fig. 2 1st cycle Li nucleation overpotential, electrodeposited Li morphology, and Li|Cu half-cell cycling performance with bare Cu and different resistive thin films modified-Cu current collectors. (a) 1st cycle Li nucleation overpotential with 8 nm Al₂O₃-Cu, 13 nm HfO₂-Cu, and 10 nm AlHf_xO_y-Cu. The error bars are calculated from three different cells. Thin film-coated Cu substrates were randomly selected from different ALD runs. 1st cycle electroplated Li⁰ morphology measured by SEM at 0.5 mA h cm⁻² capacity on (b) bare Cu, (c) 8 nm Al₂O₃-Cu, (d) 13 nm HfO₂-Cu, and (e) 10 nm AlHf_xO_y-Cu. (f) Long-term cycling performance as reported in CE with bare Cu, 8 nm Al₂O₃-Cu, 13 nm HfO₂-Cu, and 10 nm AlHf_xO_y-Cu. Experiments in a, b, and c are performed in Li|Cu half-cells using 1 M LiPF₆/EC-DEC electrolyte at 1 mA cm⁻² current density.





Fig. 3 SEI chemical composition analysis using XPS following different protocols to probe the anion-derived nature (F/C, P/C ratio), and stability (relative LiF amount) of SEI. (a) Schematic illustration of XPS sampling area of the SEI formed by protocol (i) prior to the onset of Li nucleation, using a potential hold above the Li electrodeposition potential, 10 mV vs. Li/Li⁺ for 3 h. XPS results analyzing the SEI created in protocol (i) showing (b) the F/C and P/C atomic ratios for the three different MO_x films, with the P/C range set at 1/6 of the F/C range to facilitate comparison with the 1 : 6 ratio of P : F in LiPF₆; (c) the F 1s high resolution (HR) scan for the 8 nm Al₂O₃-Cu sample; and (d) the F 1s HR scan for the 10 nm AlHf₃O₇-Cu sample. (e) Schematic illustration of XPS sampling area of the SEI formed by protocol (ii) after first cycle plating of 0.5 mA h cm⁻² Li at a current density 1 mA cm⁻². (f-h) Show the corresponding F/C and P/C atomic ratios and F 1s HR scans for protocol (ii) (i) Schematic illustration of XPS sampling area of SEI formed by protocol (iii) atop Li after first plating of 2 mA h cm⁻² Li at a current density 1 mA cm⁻². (j-l) Show the corresponding F/C and P/C atomic ratios and F 1s HR scans for protocol (iii).

there is no Li electrodeposition and thus, less Li at the surface available to react with the electrolyte and form LiF.³⁹ We also find for this protocol that the F/C and P/C ratios for AlHf₃O₇ are lower than those for Al₂O₃ and HfO₂ (Fig. 3b), suggesting that the SEI with AlHf₃O₇ coating is less anion-derived. Being organic-rich, AlHf₃O₇ would thus promote the least stable SEI,

which may explain the comparatively worse cycling performance observed for AlHf₃O₇-modified Cu (Fig. 2f). Fig. 3c and d show in the high-resolution F 1s scan that the relative LiF content is higher for AlHf₃O₇-coated Cu than for Al₂O₃-Cu; however, after accounting for the lower overall F/C ratio for AlHf₃O₇-Cu, the actual LiF/C ratio on AlHf₃O₇-Cu is shown to



be lower than on $\text{Al}_2\text{O}_3\text{-Cu}$ (ESI Table 1†), suggesting a more stable SEI for the latter.

The next protocol, protocol (ii), is the most representative of the actual cycling conditions because it is performed under similar conditions as experienced during cycling. Moreover, since sparse Li deposits are formed with resistive substrates, this experiment should show the impact of both the thin MO_x film and Li in the SEI formation. The results are shown in Fig. 3e–h. Fig. 3f shows that the average F/C ratios follow a trend $\text{Al}_2\text{O}_3\text{-Cu} > \text{HfO}_2\text{-Cu} > \text{AlHf}_x\text{O}_y\text{-Cu}$, although the differences are slighter than what is observed in Fig. 3b. We speculate that the lower degree of variation in F/C and P/C ratios in Fig. 3f than that of Fig. 3b is caused by incorporation of sparse Li deposits into the analysis. This scenario likely occurs because Li regions would induce the same SEI composition regardless of different modified copper substrates at the Li–electrolyte interface. We also observe a significantly higher proportion of LiF for protocol (ii) than for protocol (i) due to the presence of deposited Li. Within protocol (ii), the relative amount of LiF is higher for $\text{Al}_2\text{O}_3\text{-Cu}$ than for $\text{AlHf}_x\text{O}_y\text{-Cu}$ (Fig. 3g and h). This increased LiF may support the observed improved cycle life for $\text{Al}_2\text{O}_3\text{-Cu}$.

Finally, to understand the impact of only the Li surface on SEI species control, we perform an experiment with twice the deposition capacity of cycling and probe the SEI atop the Li (protocol iii). ESI Fig. 8† shows different high-resolution scans in the metal peak regions to confirm that the scans are from the regions where the probed surface is Li, *i.e.*, no metal peaks from the underlying MO_x thin films are observed in the scanning area. The results of the XPS scans for protocol (iii) are shown in Fig. 3j–l. As expected, there is no statistically significant difference among the F/C and P/C ratios measured in this experiment with different resistive substrates (Fig. 3j) because the SEI composition for this case represents predominantly the Li–electrolyte interactions. Since the F/C ratios are statistically similar, we carefully analyze the F 1s peak to find further differences in relative LiF amount. We find that a higher LiF content is observed in the Al_2O_3 -coated Cu substrate compared to $\text{AlHf}_x\text{O}_y\text{-Cu}$ (Fig. 3k and l). Although Fig. 3j–l capture the impact of Li only, a higher relative amount of LiF on $\text{Al}_2\text{O}_3\text{-Cu}$ may suggest that the $\text{Al}_2\text{O}_3\text{-Cu}$ SEI would be more stable than that of $\text{AlHf}_x\text{O}_y\text{-Cu}$.

Our results indicate that with the tested protocols to understand the SEI composition, compared to AlHf_xO_y , both Al_2O_3 and HfO_2 thin films lead to SEIs with the types of compositions typically associated with better stability. These composition features include more anion-derived SEI as measured by F/C and P/C ratios, as well as a higher proportion of F present as LiF species. This composition analysis helps explain the relative battery cycle improvement with $\text{Al}_2\text{O}_3\text{-Cu}$ and $\text{HfO}_2\text{-Cu}$ when compared to the other resistive thin film of $\text{AlHf}_x\text{O}_y\text{-Cu}$. Moreover, since protocol (ii) is the most representative of the actual cycling conditions and captures the contributions of both Li and resistive MO_x films on SEI formation, for subsequent parts of the study we investigate the SEI using protocol (ii). We speculate that different surface chemistry properties of

the thin films such as surface charge, charge density, as well as thin film deposition conditions may impact the electrolyte decomposition. The C 1s high-resolution scans of the SEIs with protocol (ii) for different substrates are shown in ESI Fig. 9.† Furthermore, to verify our argument on SEI stability, we characterize the residual SEI after the 40th stripping for our best-performing Al_2O_3 films and bare Cu. Expectedly, major differences are not observed in SEI atomic ratios (ESI Fig. 10a†) but are found in the F 1s high-resolution scans (ESI Fig. 10b†). We find a higher relative LiF content on $\text{Al}_2\text{O}_3\text{-Cu}$ compared to bare Cu substrates (ESI Fig. 10c†). These results on SEI composition are consistent with our conclusions from the initial cycle SEI characterization.

We find that both Fig. 3b and j show statistically similar values for the F/P stoichiometric ratio near ~ 6 . For the case of Fig. 3f, where both electrodeposited Li and thin film influence the salt decomposition, an off-stoichiometric F/P ratio is observed for Al_2O_3 and AlHf_xO_y interfaces. We speculate that this is due to the heterogeneity at the surface where electrodeposited Li and thin films alter the kinetics of salt decomposition differently. For Li, it is due to the electrochemical and chemical decomposition of the salt⁸ whereas, for the metal oxides the acidity of the thin films influences the salt decomposition.²

2.4. Varying the binary stacking order of resistive thin films and resulting SEI composition and performance

To better understand how the SEI composition is regulated by the metal oxide/electrolyte interface and to explore the impact of other interfaces, we employed design 2, in which two different ALD-grown metal oxides are stacked on the Cu current collector as described in Fig. 1b. Stacking the binary layered films allows for deconvolution of the impacts of the Cu/thin film interface and thin film/electrolyte interface on SEI composition and performance. For this design, we explored three different resistive MO_x films: HfO_2 , Al_2O_3 , and ZrO_2 . We introduce ZrO_2 -modified films to add another point for comparison. The thin film characterization for ZrO_2 -modified Cu substrates using XPS can be found in ESI Fig. 11,† and cycling performance test results, Li nucleation morphology, and SEI composition for the ZrO_2 samples are included in ESI Fig. 12.† The XPS results show the presence of the metallic Zr peaks, as well as an O:Zr ratio that is slightly above what is stoichiometrically expected. The cycling performance using ZrO_2 coatings (ESI Fig. 12a†) is better than bare Cu but worse than the Cu coated with Al_2O_3 and HfO_2 , with long-term coulombic efficiencies falling below 80% at 100–120 cycles. The SEM images (ESI Fig. 12b†) confirm the Li morphology remains of low surface area and planar, while the XPS high-resolution F 1s spectrum of the SEI (ESI Fig. 12d†) confirms a relatively low ratio of LiF to other fluorinated species. This result reveals that despite the Li morphology remaining similar due to the fixed resistance, the chemical nature of ZrO_2 produces a lower SEI quality and thus poorer cycling performance. The thin film characterization for the binary stack thin films on Cu using XPS can be found in ESI Fig. 13–15.† The



XPS spectra confirm that the relevant metallic peaks (Al 2p, Hf 4f, and Zr 3d) are present in the stacked films.

The thickness of each of the stacked films was selected to provide a nucleation overpotential fixed near the same value, as shown in Fig. 4a. Each half of the stack contained 4 nm Al_2O_3 , 6.5 nm HfO_2 , or 8.5 nm ZrO_2 , respectively, which correspond to half of the thickness used in the 1st cycle nucleation overpotential experiments as shown in Fig. 2a and 4a. The Li deposition across the series of stacked films continued to show low surface area, planar, resistance-fixed morphology as

shown in the SEM images in ESI Fig. 16.† This is reasonable, as our goal here is to grow thin films with equal resistance, resulting in the overall similar resistance-fixed Li morphology. We note that differences in morphology can exist due to variations in coin cell pressure distribution, spatial positioning when imaging, and thin film defect density across batches. The SEI compositions of cells modified with each of the binary MO_x stacks, as well as the single metal oxide films, were measured using XPS. The results of the F/C ratios are presented in Fig. 4b, sorted according to their thin-film electrolyte



Fig. 4 1st cycle nucleation overpotentials, F/C atomic ratios of the SEI, and F 1s HR scans of the SEI for the binary MO_x stacked films. (a) 1st cycle Li nucleation overpotential of cells modified with the stacked binary metal oxide coatings. The error bars are calculated from three different cells each. Thin film coated Cu substrates were randomly selected from different ALD runs. (b) F/C atomic ratio of SEI including cells modified with the stacked binary metal oxide coatings with protocol (ii). (c) F 1s HR scan of SEI formed using protocol (ii) on (c) Al_2O_3 on HfO_2 -Cu (d) HfO_2 on Al_2O_3 -Cu (e) Al_2O_3 on ZrO_2 -Cu and (f) ZrO_2 on Al_2O_3 -Cu.



interface. For example, Al_2O_3 , Al_2O_3 on HfO_2 , and Al_2O_3 on ZrO_2 all have the Al_2O_3 surface exposed to the electrolyte and to highlight that they form one related class of samples, their bars are positioned in front of the green background. In the F/C ratios, statistically significant differences are not observed for most films. To be specific, only two of the top-performing films, Al_2O_3 -Cu and Al_2O_3 on HfO_2 -Cu, show a statistically significant difference with the worst-performing AlHf_xO_y -Cu. Other interesting observations are that cells with the same metal oxide/electrolyte interface have similar trends in F/C ratios. For example, cells with Al_2O_3 /electrolyte interfaces have the highest F/C ratios on average, while cells with HfO_2 /electrolyte interfaces have large variances in the F/C ratio (bars positioned in front of red background). This result suggests that the SEI structure and chemical composition may be influenced by the thin film/electrolyte interface.

Since the F/C ratios themselves are not very conclusive, to gain a deeper understanding of the system, we have studied and analyzed the high-resolution XPS scans. The high-resolution F 1s peaks reveal that the ratio of the LiF peak to the C-F/ $\text{Li}_x\text{PF}_y\text{O}_z$ peak matches best with the high-resolution F 1s spectra of other films with the same metal-oxide electrolyte interface (Fig. 4c-f) as evident in the Al_2O_3 -containing interfaces. High-resolution F 1s spectra of the SEI of HfO_2 -Cu and ZrO_2 -Cu cells can be found in ESI Fig. 7b and 12d.† Cells with Al_2O_3 /electrolyte interfaces have a high LiF to C-F/ $\text{Li}_x\text{PF}_y\text{O}_z$ ratio, while those with HfO_2 /electrolyte interfaces have a similar LiF to C-F/ $\text{Li}_x\text{PF}_y\text{O}_z$ ratio, and those with ZrO_2 /electrolyte interfaces have a low LiF to C-F/ $\text{Li}_x\text{PF}_y\text{O}_z$ ratio. This corroborates that SEI composition is highly tuned by the thin film/electrolyte interface.

Long-term cycling performance tests were conducted on the cells modified with stacked thin films to explore the impact of the Cu current collector-thin film interface and thin-film electrolyte interface, as well as the aggregate stack composition, on the cell's performance and cycle life. The long-term cycling tests reveal that cells with the same metal oxide/electrolyte interface have similar performance regardless of the buried metal oxide-current collector interface (Fig. 5). A table identifying key performance parameters for each modified cell, including average CE for cycles 5–50 and the cycle index at which the cell drops below 80% CE, are reported in Table 1. The most notable differences are exemplified by the Al_2O_3 and ZrO_2 stacked set. While the cells with the Al_2O_3 /electrolyte interface have an average CE for cycles 5–50 of 84.9 (± 1.5)–87.6 (± 1.0), cells with the ZrO_2 /electrolyte interface have a statistically different average CE of 78.6 (± 1.6)–79.0 (± 0.2). Looking at more long-term performance trends, cells with the Al_2O_3 /electrolyte interface maintain CE above 80% until cycles 114 (± 43.3)–134 (± 6.6) (Fig. 5a), while cells with the ZrO_2 /electrolyte interface see CEs of <80% by 8.0 (± 1.4)–11.8 (± 7.5). The much lower values for the ZrO_2 /electrolyte interfaces could reflect a more fragile SEI that requires more cycles to stabilize. At higher cycle indices, cells with the ZrO_2 /electrolyte interface experience rapid drops in CE at 90–120 cycles (Fig. 5c), indicating less long-term stability than cells with Al_2O_3 /electrolyte or



Fig. 5 Comparative long-term cycling performance between batteries with the same thin film/electrolyte interface. Long-term cycling performance for metal oxide-modified Cu with cells containing a (a) Al_2O_3 /electrolyte interface, (b) HfO_2 /electrolyte interface, and (c) ZrO_2 /electrolyte interface. Experiments are performed in Li|Cu half-cells using 1 M $\text{LiPF}_6/\text{EC-DEC}$ electrolyte at 1 mA cm^{-2} current density.

HfO_2 /electrolyte interfaces. The long-term performance tests for the stacked thin films are each verified by at least two replicates which can be found in ESI Fig. 17.† Moreover, ESI Fig. 18† shows the comparison of CE data versus cycle index for the same material stacks (HfO_2 on Al_2O_3 versus Al_2O_3 on HfO_2) and (ZrO_2 on Al_2O_3 versus Al_2O_3 on ZrO_2) confirming that while the cycling behavior is similar for the same MO_x /electrolyte interface, it is not the same if the stack order is switched.

To show how SEI composition can impact cycling performance and SEI stability at later cycles, we include the voltage profiles for cycles 140–150 for cells modified with Al_2O_3 -Cu,



Table 1 Key performance metrics for Cu current collectors modified by varying interfacial films. Metrics are derived from performance data shown in Fig. 2 and 5, ESI Fig. 6, 12 and 17.† To avoid initial losses from SEI formation, cycles 5–80 are chosen. CE average and standard deviation values are calculated using all sequential data points using two cells for ZrO₂ and three cells for other interfaces

Film	Average CE cycles 5–50	Average CE cycles 50–80	Average CE cycles 5–80	Cycle before falling below 80% for two consecutive cycles after cycle 5
Al ₂ O ₃	87.6 ± 1.0	86.0 ± 5.9	87.0 ± 0.6	134 ± 6.6
Al ₂ O ₃ on ZrO ₂	85.9 ± 2.2	86.2 ± 1.2	86.1 ± 1.7	114 ± 43.3
ZrO ₂				
Al ₂ O ₃ on HfO ₂	84.9 ± 1.5	86.7 ± 1.5	85.6 ± 0.5	121.3 ± 29.4
HfO ₂				
HfO ₂ on Al ₂ O ₃	86.0 ± 3.3	87.7 ± 1.4	86.7 ± 2.5	124.3 ± 6.4
HfO ₂ on Al ₂ O ₃	88.2 ± 0.3	91.7 ± 5.8	89.7 ± 2.5	117 ± 9.6
Al ₂ O ₃				
ZrO ₂ on Al ₂ O ₃	79.0 ± 0.2	86.8 ± 0.4	82.1 ± 0.1	8 ± 1.4
ZrO ₂ on Al ₂ O ₃	78.0 ± 1.6	78.1 ± 7.8	78.0 ± 3.9	11.8 ± 7.5
Al ₂ O ₃				
AlHf _{1-x} O _y	90.1 ± 0.4	83.3 ± 0.8	87.4 ± 0.1	65.3 ± 11.6

Al₂O₃ on ZrO₂-Cu, and ZrO₂ on Al₂O₃-Cu in ESI Fig. 19.† Al₂O₃-Cu has a very stable voltage profile that is similar to that of Al₂O₃ on ZrO₂-Cu. Since resistance and morphology are similar, this suggests the enhanced SEI at the Al₂O₃/electrolyte interface supports performance and stabilization even at 150 cycles. Al₂O₃ on ZrO₂-Cu and ZrO₂ on Al₂O₃-Cu have the same thickness and resistance but differing thin film/electrolyte interfaces. ZrO₂ on Al₂O₃-Cu presents more instabilities reaffirming that differences in initial SEI, as confirmed by XPS, impact late-cycle stability.

To understand more about SEI stability using single and bilayer stack films, we perform electrochemical impedance spectroscopy (EIS) analysis of Li|Cu cells with electrodeposited Li for both ZrO₂ and Al₂O₃ on ZrO₂ modification (ESI Fig. 20†). We find that cells with Al₂O₃ on ZrO₂ have a higher initial SEI impedance compared to ZrO₂. We also observe a similar trend from our SEI chemical composition results where a higher average F/C ratio and a higher relative LiF content are observed with Al₂O₃/electrolyte interfaces. The trend can be rationalized with the high charge transfer resistance at the Li and resistive Al₂O₃ interface and the insulating nature of LiF causing a higher SEI resistance value consistent with previous findings on LiF-rich SEIs.¹⁰ After 25 hours, a similar degree of increase in SEI resistance (~200%) is observed with both films. This increase in SEI resistance mainly occurs from chemical SEI growth due to Li-electrolyte reactions.¹⁵ Since Li undergoes severe calendar aging and high SEI growth in the carbonate-based electrolyte, a similar degree of SEI resistance increase is observed.¹⁵ So, for this case, we believe that the SEI growth is mostly driven by electrolyte diffusion towards the surface of Li.

Our stacked film experiments clearly demonstrate that the thin film/electrolyte interface controls the SEI composition and subsequently tunes the cycling performance. These results are significant because they help decouple the impacts of the buried Cu/thin film and the exposed thin film/electrolyte inter-

faces. Whereas the SEI and cycling performance correlate with the thin film/electrolyte interface, we observe no strong correlation of either SEI or cycling performance with the buried Cu/thin film interface (ESI Fig. 21†). We postulate that the MO_x present at the Cu current collector/thin film interfaces could impact electron transport, and thus the nucleation and subsequent growth of the Li deposit.^{29,40,41} However, the cycling performance results show that the chemical composition of the MO_x at the thin film/electrolyte interface plays a dominant role due to its ability to tune the SEI composition. This result emphasizes the importance of SEI composition on the overall performance of the battery for similar types of Li morphology. Nevertheless, it is important to consider that the dominant factor for overall performance control appears to be the thin film resistance, whereas the MO_x thin film chemistry is only a secondary factor. This study intentionally removed this effect by studying MO_x thin films of equal resistance.

We note that although the cells modified with stacked films do behave similarly to cells with unstacked films that have the same thin-film electrolyte interface, the stacked films exhibited higher instability compared to the non-stacked films. This is further explored in the voltage profiles for cycles 140–150 shown in ESI Fig. 19.† Although the Al₂O₃-Cu and Al₂O₃ on ZrO₂-Cu samples have similar interfaces and similar voltage profiles, the Al₂O₃ on ZrO₂-Cu sample does have some subtle instabilities, for example at around hour 273. A previous study has shown that stacked films of Al₂O₃/HfO₂/Al₂O₃, with each layer being 20 nm, grown using ALD on stainless steel and titanium, led to the formation of agglomerates at the interlayers possibly interfering with the stability of the thin film.⁴² This could explain why, despite seeing similar coulombic efficiency trends, there is more fluctuation in the stacked films, specifically at higher cycle numbers. Additionally, despite the resistance being the same, there are up to 5 nm differences in film thickness for cells with the same thin film/electrolyte interface. This could, for example, in the case of pinhole defects, make it more difficult for Li⁺ to diffuse through the film and contact the underlying substrate. Although these differences are small, over many cycles it could impact the long-term performance. Nevertheless, the stacked film study affirms that when morphology is fixed by resistance, SEI composition regulated by the thin film/electrolyte interface is the most important predictor of battery performance.

3. Conclusions

Our results show that even with the resistance-fixed low surface area morphology of Li, different interfacial film chemistry can result in different SEI compositions, which can have different impacts on the LMB cycling performance. Due to the sparse Li morphology obtained with the resistive substrates, the thin film coated Cu surface is exposed and can impact electrolyte decomposition species in the SEI and thus modulate the average SEI composition. Interfacial thin films promoting SEIs containing more inorganic-rich and stable species



result in the most performance benefits. Specifically, Al_2O_3 and HfO_2 thin film-coated Cu result in improved cycle life in LMBs compared to AlHf_xO_y -modified Cu due to more stable SEI formation on the former. Moreover, we achieve deconvolution of Cu/thin film and thin film/electrolyte interface effects using binary stacked resistive thin films and find that the interface near the electrolyte is the crucial determinant of SEI composition and performance. By maintaining the same thin film/electrolyte interface and varying the thin film/Cu interface, we show that stacks with Al_2O_3 /electrolyte interface maintain >80% CE for ~130 cycles exhibiting similar battery cycle life and SEI compositions. Our results indicate that similar performance and chemical composition trends in the SEI are obtained for different binary stacks of thin films with the same thin film/electrolyte interface. In summary, our results identify key design concepts for tuning the SEI with fixed Li morphology using Cu interface engineering which can be beneficial for improving LMB cycle life.

4. Methods

4.1. Thin film deposition

The metal oxide thin films were deposited by ALD. For Al_2O_3 deposition, trimethylaluminum (TMA) was used as the metal-organic precursor and water (H_2O) was the counter reactant. An ALD cycling scheme of 0.03/5/0.03/30 s TMA pulse/purge/ H_2O pulse/purge sequence at 150 °C was conducted, which resulted in a 1.2 Å per cycle growth rate.

For HfO_2 deposition, tetrakis(dimethylamido) hafnium(IV) (TDMAHf) heated to 60 °C was used as the metal-organic precursor and H_2O was the counter reactant. An ALD scheme of 0.25/60/0.03/90 s TDMAHf pulse/purge/ H_2O pulse/purge sequence at 200 °C was conducted, which resulted in a 1.2 Å per cycle growth rate.

AlHf_xO_y deposition was conducted using a super cycle of the aforementioned HfO_2 deposition cycle followed by an Al_2O_3 deposition cycle. For Al_2O_3 deposition, TMA was used as the metal-organic precursor and H_2O was the counter reactant. An ALD scheme of 0.03/10/0.03/10 s TMA pulse/purge/ H_2O pulse/purge sequence was conducted. The deposition was conducted at 200 °C and resulted in a growth of 2.4 Å per cycle growth rate.

For ZrO_2 deposition, tetrakis(dimethylamido) zirconium(IV) (TDMAZr) heated to 75 °C was used as the metal-organic precursor and H_2O was the counter reactant. An ALD scheme of 2/30/1/30 s TDMAZr pulse/purge/ H_2O pulse/purge sequence at 200 °C was conducted, which resulted in a 1.1 Å per cycle growth rate.

HfO_2 , and AlHf_xO_y depositions were performed in a Gemstar 6 ALD reactor (Arradiance) reactor, while ZrO_2 and Al_2O_3 were deposited in a Veeco Savannah S200 ALD reactor. The film thickness on a witness silicon (Si) wafer was determined using a J.A Woollam M2000 Variable Angle Spectroscopic Ellipsometer at a 70° angle of incidence and wavelengths ranging from 210 to 1688 nm. All depositions were conducted on Cu foil. For stacked films, when the thin film ALD processes are conducted in different reactors,

samples were exposed to air in between sequential processes. Growth curves were studied to evaluate whether the growth behavior of the metal oxide on the silicon substrate differed from the growth behavior on a given metal oxide. Results shown in ESI Fig. 22† indicate no difference.

4.2. Electrochemistry

All battery materials were stored and assembled in an argon glovebox. The oxygen level in the argon glovebox was maintained below 0.10 ppm and water level was maintained at 0.00 ppm during all the experiments within the sensitivity of the sensor. All electrochemical processes for battery cycling tests, and to prepare samples for XPS and SEM, were performed using Li|Cu half-cells in a coin cell configuration. CR 2032 type coin cells were used. Li foil 0.75 mm thick (99.9%, Alfa Aesar) was used as the reference electrode. Li foils were mechanically scraped using commercial grade plastic battery scrapers to remove surface oxides before cell assembly. Cu foil (Pred Materials, 30 µm) was used as the working electrode. Trilayer PP/PE/PP (Celgard 2325, 25 µm) was used as the separator. 1 M $\text{LiPF}_6/\text{EC}-\text{DEC}$, or LP40, electrolyte was obtained from Gotion. 60 µL electrolyte was used in the coin cell. The cells were cycled with an Arbin battery cycler using protocols mentioned in corresponding figures. For characterization experiments, the cells were disconnected from the cycler immediately after electrochemical tests and disassembled inside the argon glovebox. After Li electrodeposition, impedance measurements were carried out within 5 minutes and after 25 hours under open-circuit conditions within a frequency range of 1 MHz to 100 mHz using a Biologic VMP3 potentiostat.

4.3. X-ray photoelectron spectroscopy (XPS)

X-ray photoelectron spectroscopy (XPS) was performed using PHI Versaprobe III, IV. The X-ray source was monochromatic Al K α . As-deposited thin films were characterized to confirm film chemistry and stoichiometry. For air-sensitive battery samples, the coin cells were disassembled inside an argon glovebox. The Cu substrates were carefully rinsed with 100 µL DEC solvent to remove any residual salt. A vacuum transfer vessel was used for transferring the samples to the XPS instrument to ensure air-free transfer. The maximum allowable Z-height for the instrument was used for spectra collection to achieve the highest signal count.

Multipak software was used for XPS data analysis. The C 1s peak at 284.5 eV was used as a reference for spectral shifting. The SEI atomic ratios were determined using the collected survey scans at 224 eV pass energy. The high-resolution signals were collected at 55 eV pass energy.

4.4. Scanning electron microscopy (SEM)

Before microscopy, all samples were rinsed with 100 µL DEC to remove residual salt and dried inside an argon glovebox. Air-sensitive battery samples were carried to the scanning electron microscope using an air-tight vessel. Samples were briefly exposed to air for a few seconds before imaging. Scanning electron microscopy was performed using Thermo Fisher Scientific Apreo S LoVac and FEI Magellan 400 XHR.



Data availability

All data needed to evaluate the conclusions in this paper are present in the main text or the ESI.†

Conflicts of interest

The authors declare no conflicts of interest.

Acknowledgements

S. F. B., S. B. S., and K. M. S. G. acknowledge support from the Stanford StorageX initiative seed grant award. S. B. S. acknowledges support from TomKat Center Graduate Fellowship for Translational Research and Link Foundation Energy Fellowship. K. M. S. G. acknowledges support from NSF GRFP. S. T. O. acknowledges support from Knight-Hennessy scholarship and TomKat Center Fellowship for Translational Research at Stanford University. Y. C. and S. B. S. acknowledge support from the Assistant Secretary for Energy Efficiency and Renewable Energy, Vehicle Technologies Office (VTO), of the U.S. Department of Energy (DoE) under the Battery Materials Research (BMR) program. Y. C. also acknowledges the support from Battery500 Consortium and CEI Consortium. We are grateful to Bang Nhan for helpful discussions on ZrO₂ ALD, and to Andreas Werbrouck for valuable discussions on thin film resistance. XPS and SEM characterizations were carried out at the Stanford Nano Shared Facilities (SNSF), supported by the National Science Foundation under the award ECCS-2026822.

References

- X.-B. Cheng, R. Zhang, C.-Z. Zhao and Q. Zhang, *Chem. Rev.*, 2017, **117**, 10403–10473.
- Y. Guo, H. Li and T. Zhai, *Adv. Mater.*, 2017, **29**, 1700007.
- M. D. Tikekar, S. Choudhury, Z. Tu and L. A. Archer, *Nat. Energy*, 2016, **1**, 1–7.
- S. B. Shuchi, S. T. Oyakhire, W. Zhang, P. Sayavong, Y. Ye, Y. Chen, Z. Yu, Y. Cui and S. F. Bent, *Adv. Mater. Interfaces*, 2024, **11**(36), 2400693.
- Z. Hao, G. Li, Y. Lu, Y. Cai, G. Yang and J. Chen, *Nano Res.*, 2023, **16**(11), 12647–12654.
- T. Li, X.-Q. Zhang, N. Yao, Y.-X. Yao, L.-P. Hou, X. Chen, M.-Y. Zhou, J.-Q. Huang and Q. Zhang, *Angew. Chem., Int. Ed.*, 2021, **60**, 22683–22687.
- D. Ruan, L. Tan, S. Chen, J. Fan, Q. Nian, L. Chen, Z. Wang and X. Ren, *JACS Au*, 2023, **3**, 953–963.
- M. S. Kim, Z. Zhang, J. Wang, S. T. Oyakhire, S. C. Kim, Z. Yu, Y. Chen, D. T. Boyle, Y. Ye, Z. Huang, W. Zhang, R. Xu, P. Sayavong, S. F. Bent, J. Qin, Z. Bao and Y. Cui, *ACS Nano*, 2023, **17**, 3168–3180.
- S. C. Kim, J. Wang, R. Xu, P. Zhang, Y. Chen, Z. Huang, Y. Yang, Z. Yu, S. T. Oyakhire, W. Zhang, L. C. Greenburg, M. S. Kim, D. T. Boyle, P. Sayavong, Y. Ye, J. Qin, Z. Bao and Y. Cui, *Nat. Energy*, 2023, **8**, 814–826.
- S. C. Kim, X. Kong, R. A. Vilá, W. Huang, Y. Chen, D. T. Boyle, Z. Yu, H. Wang, Z. Bao, J. Qin and Y. Cui, *J. Am. Chem. Soc.*, 2021, **143**, 10301–10308.
- J. Wang, W. Huang, A. Pei, Y. Li, F. Shi, X. Yu and Y. Cui, *Nat. Energy*, 2019, **4**, 664–670.
- A. B. Gunnarsdóttir, C. V. Amanchukwu, S. Menkin and C. P. Grey, *J. Am. Chem. Soc.*, 2020, **142**, 20814–20827.
- Z. Yu, H. Wang, X. Kong, W. Huang, Y. Tsao, D. G. Mackanic, K. Wang, X. Wang, W. Huang, S. Choudhury, Y. Zheng, C. V. Amanchukwu, S. T. Hung, Y. Ma, E. G. Lomeli, J. Qin, Y. Cui and Z. Bao, *Nat. Energy*, 2020, **5**, 526–533.
- M. S. Kim, Z. Zhang, P. E. Rudnicki, Z. Yu, J. Wang, H. Wang, S. T. Oyakhire, Y. Chen, S. C. Kim, W. Zhang, D. T. Boyle, X. Kong, R. Xu, Z. Huang, W. Huang, S. F. Bent, L.-W. Wang, J. Qin, Z. Bao and Y. Cui, *Nat. Mater.*, 2022, **21**, 445–454.
- D. Lin, Y. Liu, Z. Liang, H.-W. Lee, J. Sun, H. Wang, K. Yan, J. Xie and Y. Cui, *Nat. Nanotechnol.*, 2016, **11**, 626–632.
- H. Wang, Y. Li, Y. Li, Y. Liu, D. Lin, C. Zhu, G. Chen, A. Yang, K. Yan, H. Chen, Y. Zhu, J. Li, J. Xie, J. Xu, Z. Zhang, R. Vilá, A. Pei, K. Wang and Y. Cui, *Nano Lett.*, 2019, **19**, 1326–1335.
- A. Wang, X. Zhang, Y.-W. Yang, J. Huang, X. Liu and J. Luo, *Chem*, 2018, **4**, 2192–2200.
- R. Zhang, X. Chen, X. Shen, X.-Q. Zhang, X.-R. Chen, X.-B. Cheng, C. Yan, C.-Z. Zhao and Q. Zhang, *Joule*, 2018, **2**, 764–777.
- Z. Wu, C. Wang, Z. Hui, H. Liu, S. Wang, S. Yu, X. Xing, J. Holoubek, Q. Miao, H. L. Xin and P. Liu, *Nat. Energy*, 2023, **8**, 340–350.
- W. Liu, Y. Xia, W. Wang, Y. Wang, J. Jin, Y. Chen, E. Paek and D. Mitlin, *Adv. Energy Mater.*, 2019, **9**, 1802918.
- G. Huang, J. Han, F. Zhang, Z. Wang, H. Kashani, K. Watanabe and M. Chen, *Adv. Mater.*, 2019, **31**, 1805334.
- H. Zhuang, P. Zhao and Y. Xu, *Inorg. Chem. Front.*, 2020, **7**, 897–904.
- S. T. Oyakhire, W. Huang, H. Wang, D. T. Boyle, J. R. Schneider, C. de Paula, Y. Wu, Y. Cui and S. F. Bent, *Adv. Energy Mater.*, 2020, **10**, 2002736.
- Y. Zhao, L. V. Goncharova, Q. Sun, X. Li, A. Lushington, B. Wang, R. Li, F. Dai, M. Cai and X. Sun, *Small Methods*, 2018, **2**, 1700417.
- E. Kazyak, K. N. Wood and N. P. Dasgupta, *Chem. Mater.*, 2015, **27**, 6457–6462.
- S. T. Oyakhire, S.-L. Liao, S. B. Shuchi, M. S. Kim, S. C. Kim, Z. Yu, R. A. Vilá, P. E. Rudnicki, Y. Cui and S. F. Bent, *Nano Lett.*, 2023, **23**, 7524–7531.
- B. Ahmed, M. Shahid, D. H. Nagaraju, D. H. Anjum, M. N. Hedhili and H. N. Alshareef, *ACS Appl. Mater. Interfaces*, 2015, **7**, 13154–13163.
- M. Noked, C. Liu, J. Hu, K. Gregorczyk, G. W. Rubloff and S. B. Lee, *Acc. Chem. Res.*, 2016, **49**, 2336–2346.
- S. T. Oyakhire, W. Zhang, A. Shin, R. Xu, D. T. Boyle, Z. Yu, Y. Ye, Y. Yang, J. A. Raiford, W. Huang, J. R. Schneider, Y. Cui and S. F. Bent, *Nat. Commun.*, 2022, **13**, 3986.



- 30 A. J. Bard and L. R. Faulkner, *Electrochemical Methods: Fundamentals and Applications*, John Wiley & Sons, Inc., 2nd edn, 2001.
- 31 X. Yuan, B. Liu, M. Mecklenburg and Y. Li, *Nature*, 2023, **620**, 86–91.
- 32 D. T. Boyle, Y. Li, A. Pei, R. A. Vilá, Z. Zhang, P. Sayavong, M. S. Kim, W. Huang, H. Wang, Y. Liu, R. Xu, R. Sinclair, J. Qin, Z. Bao and Y. Cui, *Nano Lett.*, 2022, **22**, 8224–8232.
- 33 S. B. Shuchi, S. T. Oyakhire, W. Zhang, P. Sayavong, Y. Ye, Y. Chen, Z. Yu, Y. Cui and S. F. Bent, *Adv. Mater. Interfaces*, 2024, 2400693.
- 34 F. M. Li, B. C. Bayer, S. Hofmann, J. D. Dutson, S. J. Wakeham, M. J. Thwaites, W. I. Milne and A. J. Flewitt, *Appl. Phys. Lett.*, 2011, **98**(25), 252903.
- 35 M. D. Groner, J. W. Elam, F. H. Fabreguette and S. M. George, *Thin Solid Films*, 2002, **413**, 186–197.
- 36 M. He, R. Guo, G. M. Hobold, H. Gao and B. M. Gallant, *Proc. Natl. Acad. Sci. U. S. A.*, 2020, **117**, 73–79.
- 37 Y. S. Meng, V. Srinivasan and K. Xu, *Science*, 2022, **378**(6624), eabq3750.
- 38 J. Tan, J. Matz, P. Dong, J. Shen and M. Ye, A Growing Appreciation for the Role of LiF in the Solid Electrolyte Interphase, *Adv. Energy Mater.*, 2021, **11**, 2100046.
- 39 W. Huang, D. T. Boyle, Y. Li, Y. Li, A. Pei, H. Chen and Y. Cui, *ACS Nano*, 2019, **13**, 737–744.
- 40 S. Haghverdi Khamene, C. van Helvoirt, M. N. Tsampas and M. Creatore, *J. Phys. Chem. C*, 2023, **127**, 22570–22582.
- 41 S. Mirhashemihaghighi, J. Światowska, V. Maurice, A. Seyeux, L. H. Klein, E. Salmi, M. Ritala and P. Marcus, *Electrochim. Acta*, 2016, **193**, 7–15.
- 42 I. Spajić, E. Rahimi, M. Lekka, R. Offoiaich, L. Fedrizzi and I. Milošev, *J. Electrochem. Soc.*, 2021, **168**, 71510.

